HWAR-CHING KU and ALLAN P. ROSENBERG

PSEUDOSPECTRAL ELEMENT METHOD FOR COMPUTATIONAL FLUID DYNAMICS AND ITS PARALLEL IMPLEMENTATION

The basic equations of fluid mechanics have been known since early in the nineteenth century, but their nonlinear character has made it very difficult both to understand their general features and to predict flow evolution in specific cases. The possibility of using computers to attack such problems numerically was one of the original motivations for the development of stored-program digital computers and has remained in the forefront of large-scale computing ever since. We review here the basic ideas and report on some recent work done at the Applied Physics Laboratory.

INTRODUCTION

Classical fluid mechanics is an approximate description of nature of very wide applicability. A few drops of pond water on a microscope slide is an example, as is the universe as a whole, to a first approximation. Even though the basic equations have been known since early in the nineteenth century, their nonlinearity has so far prevented an adequate understanding of their consequences. We are often unable to predict accurately the flow evolution in very simple situations, let alone predict the weather. We do not even know if a unique continuous flow field exists at all times for each smooth initial three-dimensional flow field. Furthermore, even if an existence and uniqueness theorem is eventually established, we expect that (for most ranges of fluid parameters) two flow fields that are initially almost identical will eventually differ significantly. (It is known that the trajectories of fluid particles can be chaotic even though the velocity fields are simply time periodic at each point.) This kind of behavior poses interesting challenges to our understanding of what it means to compare theory and experiment, or even to compare ostensibly identical experiments with each other.

This article concentrates on incompressible flows—those for which the fluid density may be considered constant in space and time. The complexity of geometrically similar incompressible flows increases with the Reynolds number, $Re = UL/\nu$, where U is a typical velocity, L is a typical length scale, and ν is the kinematic molecular viscosity. Typical values of ν are 10^{-6} m^2/s for water and 15×10^{-6} m^2/s for air, both at 20°C. The following gives some typical Reynolds numbers for a few processes: swimming water mold spore, 10^{-4}; blood flow in dog's aorta, 5×10^3; Nolan Ryan's fast ball, 2×10^5; car on interstate highway, 3×10^6; and hurricane, 3×10^{11}.

Flows with high Reynolds numbers typically have motion on scales ranging from L down to small scales of the order $(L\nu^3/U^3)^{1/4}$, for which viscous effects quickly damp the motion. Thus, on the order of $Re^{9/4}$ significant degrees of freedom exist per unit volume, L^3. The interactions among all these degrees of freedom, caused by the nonlinearity of the equations of motion, make the study of fluid flow difficult. A direct numerical attack on the equations of motion requires a minimum of 8 bytes (B) of memory per degree of freedom. Even with memory costing as little as $100/MB, memory costs limit direct numerical attack to quite modest Reynolds numbers for the foreseeable future. One often, especially in engineering applications, tries to treat some or all of the degrees of freedom approximately—for example, statistically. Although such methods can be very useful, their validity and scope are very hard to judge. Techniques that appear to work well on one class of problems can fail on another, for obscure reasons. We concentrate in this article on methods of accurately solving the exact equations of motion. Methodological improvements here tend to get incorporated eventually into more approximate computations.

The desired features of numerical computations are the same, whether they are being used as an engineering tool to reduce the reliance on costly and difficult measurements, or as an aid to probing the fundamental physics of fluid flow—for example, by studying the sensitivity to small variations in the initial conditions. Because one is always interested in extending the computable range to higher Reynolds numbers, there are advantages to methods that are efficient in the amount of storage required per degree of freedom. This is true of both the storage needed to describe the flow field and any auxiliary storage needed to compute flow evolution. Since the accuracy required to distinguish physical from numerical instability increases with Reynolds number, one seeks techniques that are intrinsically accurate. As we will see in the next section, evolving the flow requires a large number of floating-point operations per time step

per degree of freedom. The running time of a computation is, therefore, a serious issue. For really large computations, the only way to keep the running time down to a reasonable level is to have multiple processors working on the problem simultaneously. Hence, one wants methods that are effective in such parallel environments. Particularly, for engineering applications, one needs methods that are able to deal with the variety of geometric shapes that occur in practice. In this article, we discuss some methods that address these goals.

The article is organized as follows: The following (second) section states the equations of motion for incompressible flow, outlines the main difficulties in understanding them, and gives a brief overview of our techniques for solving them numerically. The third section provides more details on the pseudospectral methods of representing the flow field that we employ. The fourth section explains how to break a (relatively) complicated geometry into elements with a pseudospectral expansion within each element. The fifth and sixth sections give applications to flow in bifurcating pipes and to flow over an object in a stratified fluid, respectively. The former has some relevance to blood flow.

DYNAMICAL EQUATIONS

The basic equations of fluid mechanics are the equation of mass conservation and Newton's second law applied to a lump of fluid that is macroscopically small and microscopically large. Mass conservation gives

$$\frac{\partial \rho}{\partial t} + \nabla \cdot (\rho \mathbf{u}) = 0 \, . \tag{1}$$

Here, ρ, where $\rho = \rho(\mathbf{r}, t)$, is the fluid density at a point in an inertial reference frame, and $\mathbf{u} = \mathbf{u}(\mathbf{r}, t)$ is the fluid velocity at point $\mathbf{r}$. In the important approximation in which ρ can be considered constant in space and time, this equation reduces to the condition for incompressible flow (the continuity equation):

$$\nabla \cdot \mathbf{u} = 0 \, . \tag{2}$$

Equation 2 is often applicable to liquids because they have such small compressibility that even large pressure variations produce only small density variations. It is often applicable to gas flow for speeds that are small compared with the speed of sound, because pressure variations are so small that density variations are small even though the compressibility is not.

Newton's second law applied to a lump of incompressible fluid gives the Navier–Stokes equation:

$$\frac{\partial \mathbf{u}}{\partial t} + \mathbf{u} \cdot \nabla \mathbf{u} = -\nabla p + \nu \nabla^2 \mathbf{u} + \mathbf{S} \, . \tag{3}$$

The second term on the left side of the equation arises because we are referring the velocity field to a point in space rather than to the changing position of the lump of fluid. Here p is the pressure divided by the density, ν is the kinematic viscosity, and $\mathbf{S}$ is the external forces, if any. The viscous term expresses the fact that relative motion between neighboring lumps of fluid causes them to exert frictional forces on one another. (The simple form of this term depends on the assumption that the stress is linearly related to the rate of strain [a Newtonian fluid], that the flow is incompressible, and that ν is constant.) Using some typical velocity U and length scale L to make the equation dimensionless, it can be written as

$$\frac{\partial \mathbf{u}}{\partial t} + \mathbf{u} \cdot \nabla \mathbf{u} = -\nabla p + \frac{1}{Re} \nabla^2 \mathbf{u} + \mathbf{S} \, , \tag{4}$$

where $\mathbf{u}$ has been nondimensionalized by the reference velocity, $\mathbf{U}$.

Equations 2 and 3 form a system of coupled partial-differential equations that must be completed by the specification of initial and boundary conditions. Notice that there are four equations for the four variables (pressure and the three components of velocity), but that there is no evolution equation for the pressure. Thus, it is not possible to march all four variables in a uniform fashion. The pressure is effectively a constraint linking the incompressibility condition to the evolution equations. The nonlinearity of the second term on the left of the Navier–Stokes equation and the indirectness of the pressure–velocity link are the primary factors making the consequences of the equations hard to predict. An additional subtle factor is that while the viscosity is often small, the term that it multiplies has the highest-order derivative in the equation.

After this quick look at the equations in general, we turn to methods for solving them numerically. (Two good general references are Peyret and Taylor[1] and Canuto et al.[2]) The first step is to decide on the representation of the pressure and velocity fields. Even if one knew the exact values, it would, in general, be impossible to represent them in a computer. One might approximate them, for example, by laying a Cartesian grid over space and representing the fields by their values at grid points. The next step is to define, for the approximate fields, the analog of the arithmetic operations and differentiation at a point. For example, if the fields are represented by their values at grid points, differentiation could be approximated by difference quotients of values at grid points. The final step is to decide on methods of solving the equations that result from using the approximate representation of the fields and operations in the Navier–Stokes and continuity equations.

We now give a quick overview of the methods we use to perform these steps. Space is divided into several regions. These domains do not have to be rectangular and will, in general, overlap. Each of these three-dimensional regions with curved geometry is then mapped onto a cube. The fields in the cubes are then expanded in finite sums of products of Chebyshev polynomials in each of the three coordinates. The expansion coefficients are determined so that the approximation is as accurate as

possible at selected points called the collocation points. We choose the boundaries of the physical space regions so that they may be assigned parameters by polynomials of the same order as those used to describe the fields in the cubes. Although this representation procedure is rather elaborate, it offers some significant advantages. Dividing space into multiple curvilinear regions gives both flexibility in tracking boundaries and the ability to use higher resolution in sensitive regions of the flow. Using polynomials rather than just linear functions gives higher accuracy for a given number of grid points. We usually use sixth- or eighth-order polynomials. Chebyshev polynomials have the particular advantage that the kth coefficient in the expansion of any smooth function decreases faster than any inverse power of k. Fourier expansions also have this property, but they require unrealistic periodic boundary conditions. The use of significantly higher-order polynomials (as would be necessary if we had not used multiple spatial regions) is possible, but it brings its own special set of stability problems. More details on the representation of the fields and their derivatives in terms of Chebyshev polynomials will be found in the following section, entitled Pseudospectral Methods. The section titled Isoparametric Pseudospectral Element explains the mapping between physical and computational space. In particular, it discusses some of the critical details of the way in which the fields on contiguous domains are matched.

The best approach to date for computing the time evolution of the Navier–Stokes equations is Chorin's[3] time-step splitting technique. To simplify the notation while explaining the basic ideas, we write the equations as if we could compute exact spatial derivatives and ignore questions connected with multiple domains. In Chorin's approach, explicit techniques are used to advance the velocity one time step while the new pressure is found by solving a linear partial-differential equation. The first step is to predict the solution $\bar{\mathbf{u}}$ to Equation 3 at the nth time step that would result if the pressure term were neglected for that time step and assuming that the exact value at the beginning of the time step is known. Replacing the time derivative by $(\bar{\mathbf{u}}^{n+1} - \mathbf{u}^n)/\Delta t$ gives

$$\bar{\mathbf{u}}^{n+1} = \mathbf{u}^n + \Delta t(\nu\nabla^2\mathbf{u} + \mathbf{S} - \mathbf{u} \cdot \nabla\mathbf{u})^n , \tag{5}$$

where the superscript n denotes the nth time step. The size of a stable time step can be increased by using an adaptation of Runge–Kutta techniques.[4] The second step is to develop the pressure and corrected velocity fields that satisfy the continuity equation by using the relationships

$$\mathbf{u}^{n+1} = \bar{\mathbf{u}}^{n+1} - \Delta t\nabla p \tag{6a}$$

$$\nabla \cdot \mathbf{u}^{n+1} = 0 . \tag{6b}$$

An equation for the pressure can be obtained by taking the divergence of Equation 6a. In view of Equation 6b, one sees that

$$\nabla^2 p = \frac{\nabla \cdot \bar{\mathbf{u}}^{n+1}}{\Delta t} . \tag{7}$$

If p satisfies Equation 7, then $\mathbf{u}^{n+1}$ does indeed satisfy Equation 6b. The solution of the pressure Poisson equation (Equation 7) is the most computationally expensive step. For some simple geometries it can be directly solved numerically by separation of variables. In general, there is no simple method for direct solution, and one must resort to iterative techniques. The quality of a solution is directly related to the accuracy with which the incompressibility condition is satisfied. Equation 7 is of the general form

$$Lp = S \tag{8}$$

for some linear operator L on some finite dimensional vector space. The properties of the operator L depend on the methods chosen to represent the fields and their derivatives. Very effective techniques are known in the event that L is positive definite symmetric. The problem can then be reduced to minimizing the real-valued function J defined by

$$J(p) = (p, Lp) - (p, S) , \tag{9}$$

where $(\ ,\ )$ denotes the inner product. The efficiency derives from two key ideas. One is that in the basic iteration relating the $k + 1$th approximation to the kth,

$$p^{k+1} = p^k + \alpha_k h^k , \tag{10}$$

steepest-descent methods are improved by imposing orthogonality conditions on the successive directions, h. For the conjugate residual method,[5] the condition is that

$$(Lh^{k+1}, Lh^k) = 0 , \tag{11}$$

whereas α_k is chosen so that p^{k+1} minimizes the Euclidean norm of the residual

$$r^k = S - Lp^k . \tag{12}$$

It can be shown that the number of iterations required for convergence is proportional to the square root of κ, the spectral condition number, where κ is the ratio of the maximum to the minimum eigenvalues. The other key idea is to actually solve a related problem with a smaller condition number whose solution can be easily related to that of the original problem. This technique is called preconditioning. In general, the operators L arising in our work are not positive definite symmetric. There is little general theory for operators that are not positive definite symmetric, but it has nonetheless often proved possible[6]

to use preconditioned conjugate residual methods. We have adapted them to our work as follows: Instead of Equation 8, we solve

$$L_{ap}^{-1} Lp = L_{ap}^{-1} S , \tag{13}$$

where L_{ap} is an approximate operator with nice properties.[7] The iterative procedure then reads as follows:

Given p^0, compute $r^0 = S - Lp^0$, $z^0 = L_{ap}^{-1} r^0$, $h^0 = z^0$. Then, for $k = 0, 1, 2, \ldots$, until $\|r^k\| < \epsilon$, do

$$p^{k+1} = p^k + \alpha^k h^k , \tag{14a}$$

$$r^{k+1} = r^k - \alpha^k L h^k , \tag{14b}$$

$$z^{k+1} = L_{ap}^{-1} r^{k+1} , \tag{14c}$$

$$h^{k+1} = z^{k+1} - \beta^k h^k , \tag{14d}$$

where

$$\alpha^k = \frac{(r^k, Lh^k)}{(Lh^k, Lh^k)} , \qquad \beta^k = \frac{(Lz^{k+1}, Lh^k)}{(Lh^k, Lh^k)} . \tag{15}$$

Here (,) denotes the inner product. Let $\mathbf{z}^k$ in Equation 14c, $k \geq 1$, be expanded in a series of eigenfunctions such that

$$\mathbf{z}^k = \mathbf{E}\xi \hat{\mathbf{z}}^k \mathbf{E}\eta^T \mathbf{E}\zeta^T , \tag{16a}$$

and similarly let the residual $\mathbf{r}^k$ be expanded such that

$$\mathbf{r}^k = \mathbf{E}\xi \hat{\mathbf{r}}^k \mathbf{E}\eta^T \mathbf{E}\zeta^T . \tag{16b}$$

Then the three-dimensional preconditioner can be reduced to the simple algebraic equation

$$(\alpha_i + \beta_j + \gamma_k)\, \hat{z}^k_{i,j,k} = \hat{r}^k_{i,j,k} , \tag{17}$$

where α_i, β_j, and γ_k are the eigenvalues with respect to separable derivative operators of the preconditioner, and $\mathbf{E}\xi$, $\mathbf{E}\eta$, and $\mathbf{E}\zeta$ are the corresponding eigenvectors associated with each eigenvalue. If there are N degrees of freedom in each direction, the overall memory required for finding the solution to the pressure Poisson equation in three dimensions is $O(N^3)$. This is the same type of maximally storage-efficient scaling that we have for the velocity field.

We have so far glossed over the problems of solving for the pressure on multiple overlapping domains. The difficult problem here is that if one has solved for the pressure in one domain, the interior values in it have to be used to get the boundary values for a contiguous domain while trying to ensure that the continuity equation is satisfied as nearly as possible at points that are common to the interior of both domains. We have discussed the problems of solving for the pressure on multiple overlapping domains for Cartesian coordinates in Refs. 4 and 8.

Most of our work has been done on a computer with four processors, but we believe that, for large computations, the future belongs to machines that have on the order of a hundred to a million processors. Although we have not yet had the opportunity to try our techniques on such machines, we think that they can be implemented nicely on such machines. Despite the inevitably messy details connected with the use of multiple curvilinear domains, the bulk of our programs can be concisely described in terms of dot products and matrix multiplication between subsets of arrays. Although cumbersome to write in older Fortran, they are specified simply in the draft international standard for the newest version of the language. Our programs, in fact, completely conform to the new standard. Thus, they will run without source code changes on any machine having a compiler implementing the newest version of the language. Once the standard is adopted (which is likely to occur within the next few months), they will run essentially on any commercially available machine intended for general-purpose scientific processing. Our programs will not necessarily run efficiently on any particular machine; however, given the centrality of the essential operations to the new version of the language, we think they will be reasonably efficient on most machines.

PSEUDOSPECTRAL METHODS

We now want to give some of the details of the way in which we represent the pressure and velocity fields. Spectral methods, which are the extension of the technique of separation of variables, have long been advocated by Orszag[9] for the solution of partial differential equations. In these methods, the partial derivatives of dependent variables are calculated from truncated series expansions of the variable in terms of smooth (usually orthogonal) functions. In pseudospectral methods, the expansions of the dependent variables in terms of smooth functions are carried out according to the method of selected points (collocation). The choice of collocation points, although not crucial, can be made in ways that make the calculation convenient and accurate. Spectral methods are also the simplest weighted-residual methods; in other words, the residual (the difference between the approximate and the real solutions) is zero at the specified points. A natural expansion for a periodic function is its Fourier series. The convergence of a truncated Fourier series depends on the smoothness of the function as well as its behavior at the boundaries. Non-

periodic functions are approximated by truncated Chebyshev polynomial expansions. Thus, a nonperiodic function f, whose interval of definition can be mapped onto $[-1, 1]$—the set of values of x between -1 and $+1$—is expanded by a finite series of Chebyshev polynomials, $T_k(x)$, as

$$f(x) = \sum_{k=0}^{N} a_k T_k(x) . \tag{18}$$

If the function is evaluated at the collocation points, $x_j = \cos \pi j/N$ (the extrema of Chebyshev polynomials), $j = 0, \ldots, N$, then the expansion in Equation 18, in view of the property

$$T_k(\cos \theta) = \cos k\theta , \tag{19}$$

reduces to the Fourier series expansion

$$f(x_j) = \sum_{k=0}^{N} a_k \cos \frac{\pi kj}{N} , \tag{20}$$

where the expansion coefficient, a_k, is given by

$$a_k = \frac{2}{N\bar{C}_k} \sum_{j=0}^{N} \bar{C}_j^{-1} T_k(x_j) f(x_j) , \tag{21}$$

$\bar{C}_0 = \bar{C}_N = 2$, and $\bar{C}_k = 1$ for $1 \le k \le N - 1$. The convergence of the Chebyshev expansion depends only on the smoothness of the function in the interior irrespective of its boundary behavior. The derivatives of $f(x)$ are calculated from the relations

$$f'(x_j) = \sum_{k=0}^{N} a_k^{(1)} T_k(x_j) \tag{22a}$$

$$f''(x_j) = \sum_{k=0}^{N} a_k^{(2)} T_k(x_j) , \tag{22b}$$

where $a_k^{(1)}$ and $a_k^{(2)}$ are expanded in terms of a_k by the recursive relation

$$c_{k-1} a_{k-1}^{(q)} - a_{k+1}^{(q)} = 2k a_k^{(q-1)} , \quad k > 1, \quad q = 1, 2 , \tag{23}$$

where $c_0 = 2$, and $c_k = 1$ for $k \ge 1$.

Alternatively, the derivatives of $f(x)$ at the points x_j can be expressed in terms of a field variable, $f(x_j) \equiv f_j$, evaluated at the same points, that is approximated by

$$f'(x_j) = \sum_{n=0}^{N} \hat{G}_{j,n}^{(1)} f_n \tag{24a}$$

$$f''(x_j) = \sum_{n=0}^{N} \hat{G}_{j,n}^{(2)} f_n . \tag{24b}$$

Here $\hat{\mathbf{G}}^{(q)} = \mathbf{T}\mathbf{G}^{(q)}\hat{\mathbf{T}}$, $q = 1, 2$, and $\mathbf{G}^{(2)} = \mathbf{G}^{(1)}\mathbf{G}^{(1)}$, where $\mathbf{T}$ and $\mathbf{G}^{(1)}$ are $(N + 1) \times (N + 1)$ matrices with elements

$$T_{k,j} = \cos \frac{\pi kj}{N} \tag{25a}$$

$$G_{k,j}^{(1)} = \begin{cases} 0 & k \ge j \text{ or } k + j \text{ is even} \\ 2j/C_k & \text{otherwise } (C_0 = 2, C_k = 1 \text{ for } k \ge 1) , \end{cases} \tag{25b}$$

and $\hat{\mathbf{T}}$ is the inverse Fourier cosine series

$$\hat{T}_{k,j} = \frac{2}{N\bar{C}_k\bar{C}_j} \cos \frac{\pi kj}{N} \tag{25c}$$

($\bar{C}_0 = \bar{C}_N = 2$, and $\bar{C}_k = 1$ for $1 \le k \le N - 1$) .

The advantages of the pseudospectral method are summarized as follows:

1. Whereas resolution of a problem with a boundary layer of thickness ϵ requires $O(1/\epsilon)$ uniformly spaced points using finite difference methods, it requires only $O(1/\sqrt{\epsilon})$ terms of the Chebyshev expansion in the pseudospectral method.

2. Terms involving nonconstant coefficients and nonlinearities are calculated in whichever representation—physical or spectral space—is most convenient.

3. The programming effort for the calculation of partial derivatives, fast Fourier transform, or matrix multiply is as simple as finite difference methods; however, the accuracy attained by the high-order Chebyshev polynomials is much higher than that of low-order finite difference methods.

Using a global Chebyshev expansion for the entire physical domain leads to both a small time step and an increased sensitivity to oscillating overshoot (Gibbs phenomenon). These Gibbs oscillations cannot be smoothed out by filtering techniques; instead, they can be alleviated by dividing the domain into a small number of elements (subdomains or pseudospectral elements) where a piecewise Chebyshev expansion with continuity of the function and satisfaction of the equation of motion at the element–element interface[8] is used to calculate the derivatives. The use of multiple elements also allows a larger time step. It can be increased still further by the use of a higher-order time integration scheme. We now elaborate on decomposing space into multiple domains.

ISOPARAMETRIC PSEUDOSPECTRAL ELEMENT

Let us first define the existence of a mapping function between the physical space (x, y, z) and the computational space (ξ, η, ζ) (a transformed space with Cartesian

coordinates). Once such coordinate relationships are known, shape functions defining geometry can be specified in local coordinates, and a one-to-one correspondence between Cartesian and curvilinear coordinates can be established. An isoparametric mapping, as defined earlier, is applied to map a three-dimensional curved geometry (physical space) onto a cube (computational space). The main objective of the present development is to provide the three-dimensional computational grids around complex geometries in a structured fashion. The pseudospectral element grid-generation scheme presented here uses a multiple block structure; the global computational domain based on the geometrical configuration is divided into a few blocks, and each block is then arbitrarily partitioned by the pseudospectral elements. The grid generation is performed in two levels. First, each block is defined as a parent element, of which the shape can be defined by a curved isoparametric pseudospectral element. Next, appropriate family elements linearly (or higher-order) interpolating the shape function of their parent elements are allocated within each of these blocks. In other words, a cubic element that contains $N\xi + 1$, $N\eta + 1$, and $N\zeta + 1$ collocation points $[\xi_i = \cos(\pi i/N\xi)$, $\eta_j = \cos(\pi j/N\eta)$, $\zeta_k = \cos(\pi k/N\zeta)]$, in the transformed space, $-1 \le \xi \le 1$, $-1 \le \eta \le 1$, $-1 \le \zeta \le 1$ (Fig. 1), corresponds to an irregular or regular six-faced (hexahedral) element in the physical space. For an isoparametric mapping, once the collocation points (x, y, z) along the curving boundaries of each parent element are known, the interior points (including the boundaries of family elements) are interpolated by deforming the (ξ, η, ζ) mesh into its (x, y, z) image using the "trilinear blending function";[10] that is, the grid points $(x, y, z)_{ijk}$ in the physical space are mapped onto $(\xi = \xi_i, \eta = \eta_j, \zeta = \zeta_k)$ in the transformed space. Figure 1 summarizes the technique of an isoparametric mapping for grid generation:

If we let ϕ be any value of (x, y, z), the interpolation translates the Boolean sum[11] into the form

$$\phi = P_\xi\phi + P_\eta\phi + P_\zeta\phi - P_\xi P_\eta\phi - P_\xi P_\zeta\phi - P_\eta P_\zeta\phi + P_\xi P_\eta P_\zeta\,\phi\,, \tag{26}$$

where the "projectors," P_ξ, P_η, and P_ζ, interpolate ϕ between two opposing faces of the six-sided region; the double-product projector, $P_\xi P_\eta$, interpolates ϕ in two directions from the four edges along which ξ and η are constant; and the triple-product projector, $P_\xi P_\eta P_\zeta$, interpolates ϕ from the eight corners. With linear interpolation functions defined as

$$N^{(1)}(\xi) = \frac{1+\xi}{2}, \quad N^{(2)}(\xi) = \frac{1-\xi}{2}$$

$$N^{(1)}(\eta) = \frac{1+\eta}{2}, \quad N^{(2)}(\eta) = \frac{1-\eta}{2}$$

$$N^{(1)}(\zeta) = \frac{1+\zeta}{2}, \quad N^{(2)}(\zeta) = \frac{1-\zeta}{2}, \tag{27}$$

the explicit expressions for the face projectors are

$$P_\xi\phi = N^{(1)}(\xi)\phi(1, \eta, \zeta) + N^{(2)}(\xi)\phi(-1, \eta, \zeta)$$

$$P_\eta\phi = N^{(1)}(\eta)\phi(\xi, 1, \zeta) + N^{(2)}(\eta)\phi(\xi, -1, \zeta)$$

$$P_\zeta\phi = N^{(1)}(\zeta)\phi(\xi, \eta, 1) + N^{(2)}(\zeta)\phi(\xi, \eta, -1)\,, \tag{28}$$

and the edge projectors are

$$\begin{aligned} P_\xi P_\eta\phi = {} & N^{(1)}(\xi)N^{(1)}(\eta)\phi(1, 1, \zeta) \\ & + N^{(1)}(\xi)N^{(2)}(\eta)\phi(1, -1, \zeta) \\ & + N^{(2)}(\xi)N^{(1)}(\eta)\phi(-1, 1, \zeta) \\ & + N^{(2)}(\xi)N^{(2)}(\eta)\phi(-1, -1, \zeta) \end{aligned}$$

$$\begin{aligned} P_\xi P_\zeta\phi = {} & N^{(1)}(\xi)N^{(1)}(\zeta)\phi(1, \eta, 1) \\ & + N^{(1)}(\xi)N^{(2)}(\zeta)\phi(1, \eta, -1) \\ & + N^{(2)}(\xi)N^{(1)}(\zeta)\phi(-1, \eta, 1) \\ & + N^{(2)}(\xi)N^{(2)}(\zeta)\phi(-1, \eta, -1) \end{aligned}$$

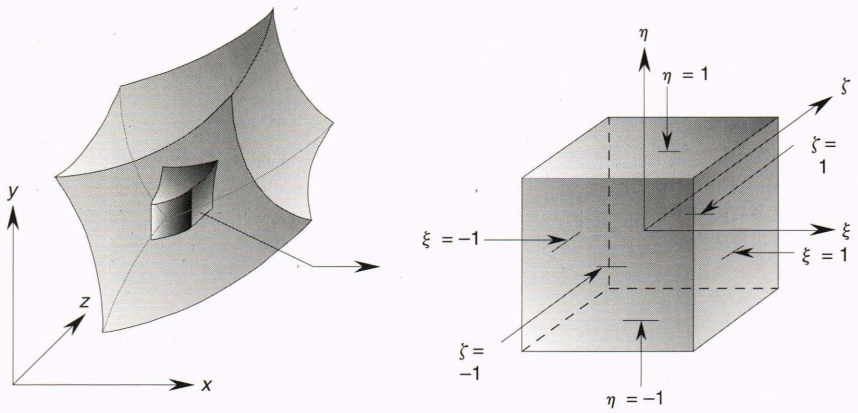

Figure 1. Three-dimensional isoparametric mapping of family elements.

$$P_\eta P_\zeta \phi = N^{(1)}(\eta)N^{(1)}(\zeta)\phi(\xi, 1, 1) + N^{(1)}(\eta)N^{(2)}(\zeta)\phi(\xi, 1, -1) + N^{(2)}(\eta)N^{(1)}(\zeta)\phi(\xi, -1, 1) + N^{(2)}(\eta)N^{(2)}(\zeta)\phi(\xi, -1, -1) , \quad (29)$$

and the corner projector is

$$\begin{aligned} P_\xi P_\eta P_\zeta \phi = {} & N^{(1)}(\xi)N^{(1)}(\eta)N^{(1)}(\zeta)\phi(1, 1, 1) \\ & + N^{(1)}(\xi)N^{(1)}(\eta)N^{(2)}(\zeta)\phi(1, 1, -1) \\ & + N^{(1)}(\xi)N^{(2)}(\eta)N^{(2)}(\zeta)\phi(1, -1, -1) \\ & + N^{(1)}(\xi)N^{(2)}(\eta)N^{(1)}(\zeta)\phi(1, -1, 1) \\ & + N^{(2)}(\xi)N^{(1)}(\eta)N^{(1)}(\zeta)\phi(-1, 1, 1) \\ & + N^{(2)}(\xi)N^{(1)}(\eta)N^{(2)}(\zeta)\phi(-1, 1, -1) \\ & + N^{(2)}(\xi)N^{(2)}(\eta)N^{(1)}(\zeta)\phi(-1, -1, 1) \\ & + N^{(2)}(\xi)N^{(2)}(\eta)N^{(2)}(\zeta)\phi(-1, -1 , -1) , \quad (30) \end{aligned}$$

where the surface function $\phi(\xi, \eta, 1)$ can be adequately represented by an isoparametric tensor product such that

$$\phi(\xi, \eta, 1) = \sum_{i=0}^{N} \sum_{j=0}^{N} N_i(\xi)N_j(\eta)\phi(\xi_i, \eta_j, 1) , \quad (31)$$

and similarly for the edge function $\phi(\xi, 1, 1)$,

$$\phi(\xi, 1, 1) = \sum_{i=0}^{N} N_i(\xi)\phi(\xi_i, 1, 1) , \quad (32)$$

Here $N_i(\xi)$ and $N_j(\eta)$, the shape functions of each parent element derived from the Chebyshev polynomials, read

$$N_i(\xi) = \sum_{m=0}^{N} T_m(\xi)\hat{T}_m(\xi_i) \quad (33a)$$

$$N_j(\eta) = \sum_{n=0}^{N} T_n(\eta)\hat{T}_n(\eta_j) , \quad (33b)$$

where the matrices $T_m(\xi)$ and $\hat{T}_m(\xi)$ have been defined by Equation 19 and Equation 25, respectively. The shape functions $N_i(\xi)$ and $N_j(\eta)$ satisfy the Kronecker-delta property, that is, $N_i(\xi_m) = \delta_{im}$, $N_j(\eta_n) = \delta_{jn}$.

In an analogous manner, other undefined surface and edge functions can be derived without any difficulty. It is obvious that Equation 26 interpolates the surface boundary functions exactly.

BIFURCATION BLOOD FLOW

Flows in branching tubes occur in many situations. In particular, they appear in the human carotid artery and aorta. Fluid dynamics helps us to understand the characteristics of such flows and their possible physiological consequences.[12]

It is typical in such flows that there will be regions near the branch points where the flow circulates around a stagnant region. Examples are shown in Figures 2 and 3. The location of the flow recirculation zone (low shear region) plays a significant role in the early stages of atherosclerotic lesions. Two-dimensional flow models only provide a simple view of this problem, and many of the important effects cannot be adequately described by them.

Figure 4 roughly represents the three-dimensional human carotid bifurcation configuration. A simplified bifurcation model (Fig. 5) is adopted here because of the lack of actual representation of the carotid artery. A steady flow instead of pulsatile flow at the entrance is assumed for simplicity. For the two-dimensional bifurcating flow, the characteristic velocity and length defining the Reynolds number, $Re = UL/\nu$, are based on the maximum velocity U and half-width of the upstream channel L. We have allocated 10×4 elements (six points per element) in the streamwise and transverse directions along each channel.

For $Re = 500$ with a branching angle of 90° (symmetry condition), the flow separates immediately from the upper or lower wall of each branch, and the maximum stream function is $\psi_{max} = 1.3484$ (Fig. 2). The quantity ψ is defined by $u_x = \partial\psi/\partial y$ and $u_y = -\partial\psi/\partial x$, where u is the horizontal velocity. For asymmetric bifurcation flow, if the flow rate is initially specified at each branch, the total pressure drop from the entrance to the exit along each channel is not the same.

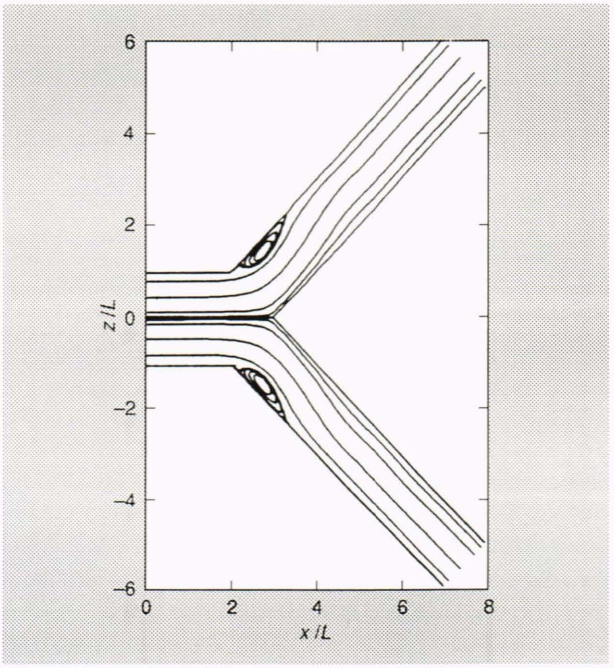

Figure 2. Streamline pattern for the symmetric bifurcation flow at a Reynolds number of 500. The dimension L is the half-width of the channel.

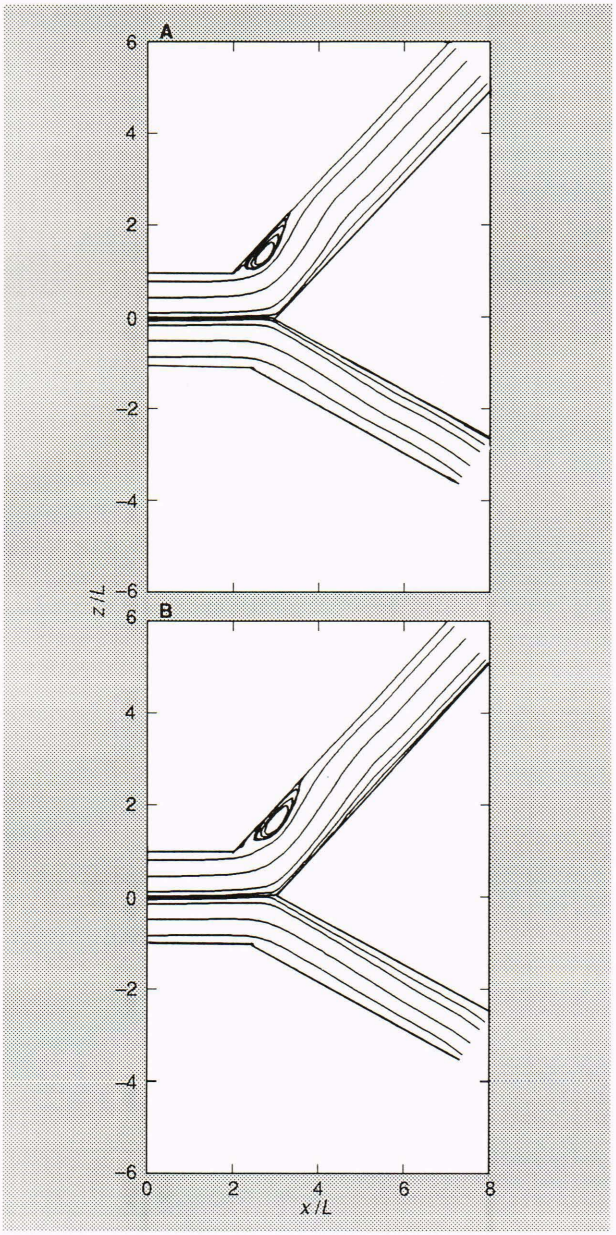

Figure 3. Streamline pattern for the asymmetric bifurcation flow at a Reynolds number of 500. **A**. The half flow rate is specified. **B**. The flow rate is adjusted (compatible pressure drop) along each branch. The dimension L is the half-width of the channel.

Figure 3A shows an asymmetric branch for $Re = 500$ and a branching angle of 71.5°, with each branch containing half the flow rate of the upstream channel. The resulting streamlines ($\psi_{max} = 1.3503$ in the upper branch) are very similar to those of Figure 2, except for a strong downward current existing in front of the bifurcation point; however, the total pressure variation in the upper channel (0.06756) differs from that of the lower one (–0.01398). Hence, the flow rate along each branch needs to be adjusted so that the total pressure drop along each channel is compatible. Since the relation between the total pressure drop and the flow rate is quasi-linear, following Newton's method, the corrected flow rate

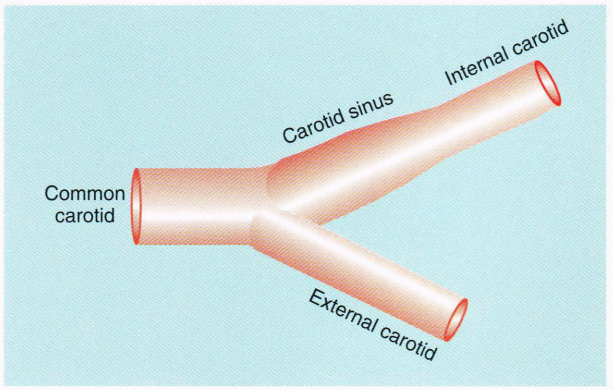

Figure 4. Three-dimensional representation of human carotid bifurcation.

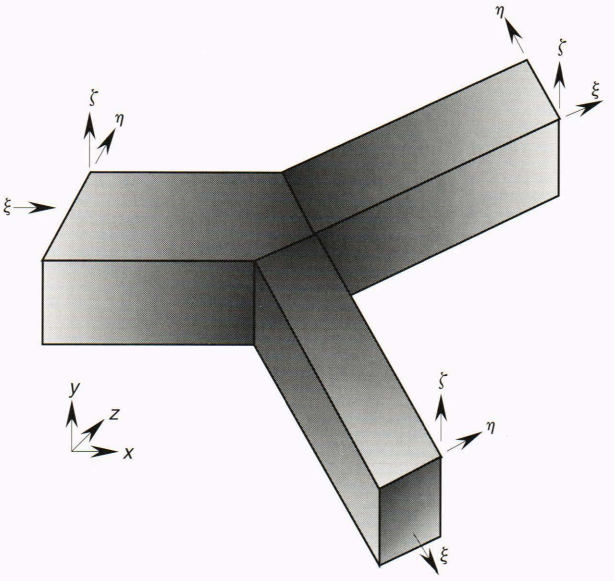

Figure 5. Simplified three-dimensional bifurcation model and coordinate system.

along each branch can be adequately determined by a few iterations.

Figure 3B shows the modified streamlines ($\psi_{max} = 1.3536$ in the upper branch) by imposing the constraint that the same total pressure drop ($\Delta p = 0.0134$) along each channel can be reached. Figure 3B also indicates that the separation along the upper branch has been deferred to a further downstream position because of the switching flow from the lower one. Similarly, the reattachment length is slightly increased.

For the three-dimensional bifurcation flow, only the symmetric condition was examined. With a uniform depth of $\sqrt{2}\,L$ in the spanwise direction, the multi-block scheme is shown in Figure 6. In addition to having the same number of elements in the streamwise (ξ) and transverse (ζ) directions as in the two-dimensional flow, three elements were used in the spanwise direction (η). As expected, because of the finite domain in the spanwise direction, the three-dimensional velocity profiles deviate from the two-dimensional ones. This result is ap-

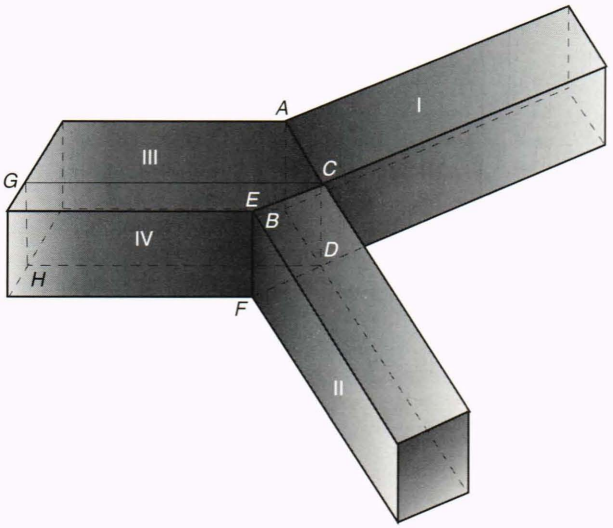

Figure 6. Three-dimensional configuration of domain decomposition (multiple blocks), showing the number and letter designations used for computational purposes.

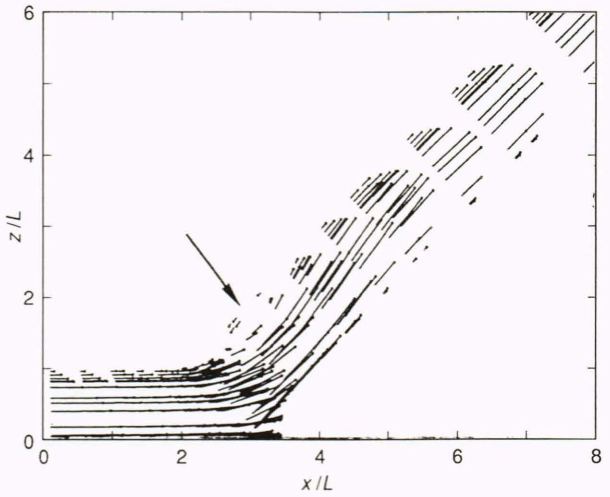

Figure 8. Velocity vectors for a Reynolds number of 500 in two-dimensional flow. The dimension L is the half-width of the channel.

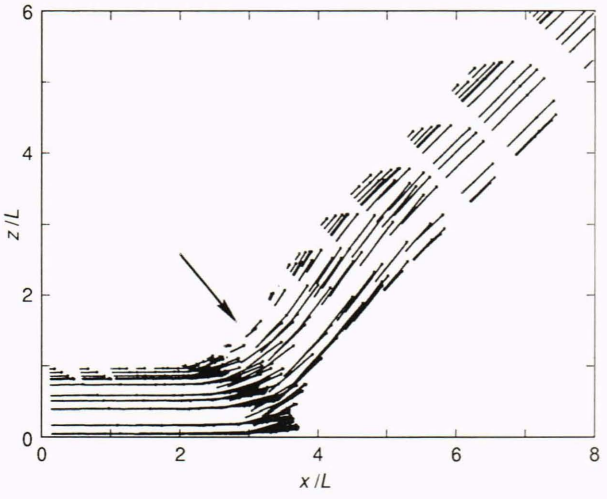

Figure 7. Velocity vectors for a Reynolds number of 500 in three-dimensional flow along the central plane (η = 0.707, where η is the spanwise direction). The arrow indicates the flow separation zone where early atherosclerotic lesions tend to occur. The dimension L is the half-width of the channel.

parent in comparing the velocity vectors of the three-dimensional flow (Fig. 7) along the central plane (η = 0.707) with those of the two-dimensional flow (Fig. 8). The separation appearing in the two-dimensional flow becomes weak in the three-dimensional flow. This weakening occurs because the higher flow rate in the central plane (η = 0.707) of the three-dimensional flow causes thinner boundary layers along the upper wall of the branch.

INTERNAL WAVES

We now look at some examples that go beyond the constant-density approximation. In many geophysical situations, the density is approximately constant in the horizontal but varies in the vertical. The Boussinesq approximation is very useful in such situations, neglecting such variations except in the term giving the gravitational force. We use the approximation here to discuss the internal waves that arise when a density-stratified fluid is disturbed. These waves generalize ordinary surface waves that can be thought of as occurring in a fluid with only two densities—those of air and water. Such waves can be remotely sensed by synthetic aperture radar. Here we focus on two types: internal waves generated by the collapse of the wake left behind by a submerged body moving in a stratified fluid, and those generated by the moving submerged body itself. The latter case is more complicated to analyze because surface and internal waves interact with the primary flow field.

Wake Collapse

Experiments conducted by Wu[13] have demonstrated the collapse of a mixed region in a linearly density-stratified fluid, and his experimental results adequately describe the visible and often spectacular effects of internal gravity waves. He also described three stages by which the perturbed fluid seeks its equilibrium density level. In such phenomena, an oscillating flow of energy occurs from potential to kinetic and back. To capture this effect accurately, we use a fourth-order Runge–Kutta time-integration scheme,[4] which does a good job of conserving energy in the following simple test problem. When an inviscid density-stratified fluid in a square box with each side of length 6 is disturbed by a Gaussian density perturbation, $\rho' = -(\rho_0)_y\,(y - y_c)\exp[-0.693(r/r_c)^2]$, where $r_c = 0.5$, $y_c = 3$, and $(\rho_0)_y = -0.003134$, the division of the total energy into potential energy (PE),

$$PE = -\frac{g}{2}(\rho_0)_y \int\int_A (\rho')^2\, dx\, dy\,, \qquad (34)$$

and kinetic energy (KE),

$$KE = \frac{1}{2} \int \int_A (\rho_0 + \rho')(u^2 + v^2)\, dx\, dy\,, \qquad (35)$$

will vary with time. Figure 9 sketches the energy versus the Brunt–Väisälä period, $Nt/2\pi$ ($N = [(-g/\rho_0)(\partial\rho_0/\partial y)]^{1/2}$). The Brunt–Väisälä or buoyancy frequency, N, is the angular frequency with which a fluid particle displaced vertically will oscillate about its original position. The total energy is conserved with 0.28% error at eight Brunt–Väisälä periods.

We now apply this technique to a numerical simulation similar to Wu's experiment. A fluid with a linear density gradient, $(-1/\rho^*)(\rho_0)_y = 0.00025$ cm^{-1} (ρ^* is a reference density, 1 g/cm^3), is confined within a rigid tank about 440 cm long and 120 cm high. A uniformly mixed circular region with a radius of 15.6 cm was placed in the middle of the tank as an initial disturbance. The top surface is assumed to be a stationary free surface (no shear stress); that is, the fluid is allowed to develop along the horizontal direction. Internal waves generated by an initial collapse of the mixed region result in the displacement of a fluid particle away from its equilibrium state (density change), and consequently causes an oscillatory motion. Flow patterns can be represented by moving rays connecting either crests or troughs. These rays originate from the collapse center and decrease their slopes when moving away from the core region. Such phenomena can be clearly visualized by the evolution of isopycnic (constant density) lines as shown in Figure 10 at the times Nt = 3, 6, 9, and 12.

Submerged Body Moving in a Thermocline

When the fluid is stratified, the wake patterns around a moving obstacle significantly differ from those in a homogeneous fluid. Two key parameters account for most features of flow motion—the Reynolds number, $Re = UL/\nu$, and the Froude number, $Fr = U/NL$, where U is the body speed and L is the characteristic length. For large values of Re and Fr, the effect of stratification is expected to be relatively unimportant; however, if the Brunt–Väisälä frequency, N, is dominant (small Fr), the

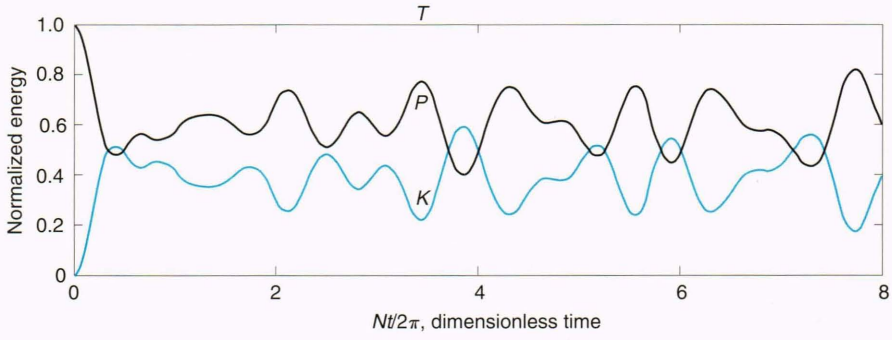

Figure 9. Energy partition versus Brunt–Väisälä period, $Nt/2\pi$. The line, *T*, indicates the normalized total energy, whereas the black line, *P*, and the blue line, *K*, are the potential and kinetic energies, respectively.

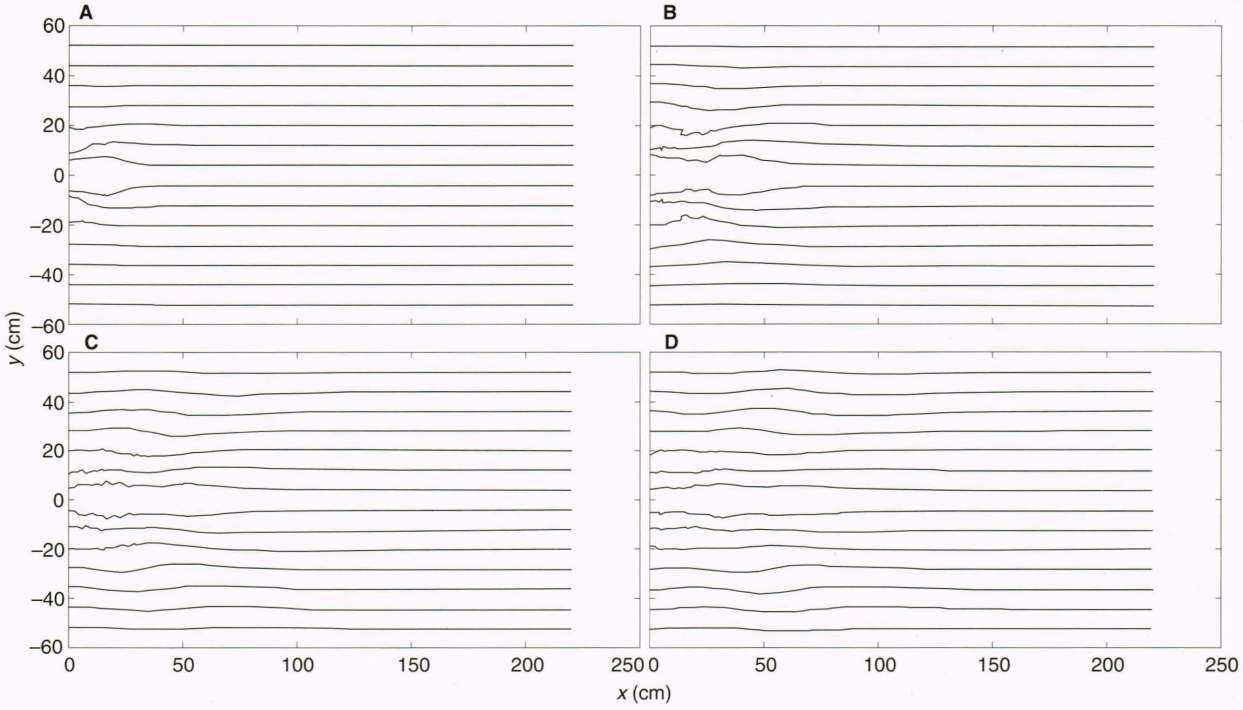

Figure 10. Isopycnic lines at various times, *Nt*. **A**. Nt = 3. **B**. Nt = 6. **C**. Nt = 9. **D**. Nt = 12.

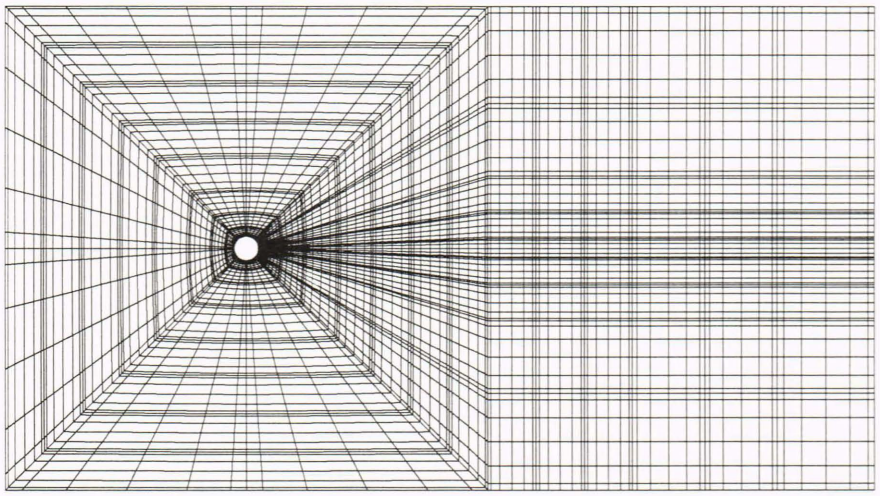

Figure 11. Layout of computational grids for flow over a cylinder.

strong stratification will distort the wake in front of and behind a moving obstacle and will tend to suppress vortex shedding behind an obstacle. When such conditions exist, the transport of mass, momentum, and energy by turbulent eddy mixing requires more work against the effective gravitational field by consuming the kinetic energy; hence, the vertical motion is inhibited. The effect of lee waves on the wake of an obstacle is more pronounced as the Reynolds number becomes smaller. In a realistic environment, a moving obstacle will be situated in one of three vertical regions: above (top mixing layer), below (weak density gradient), or within a thermocline, and the resulting flow fields will be different for each region.

A numerical experiment was conducted by horizontally moving a cylinder in a linear density-stratified fluid at $Re = 100$ (based on the diameter of a cylinder). The gridding generated by the isoparametric pseudospectral element method is plotted in Figure 11. The vortex shedding behind a cylinder in a homogenous fluid ($Fr = \infty$ in Fig. 12A) is compared with stratified fluids at $Fr = 1.15$ (Fig. 12B) and $Fr = 0.77$ (Fig. 12C). The vortex shedding, as expected, is gradually inhibited by continuously increasing the Brunt–Väisälä frequency.

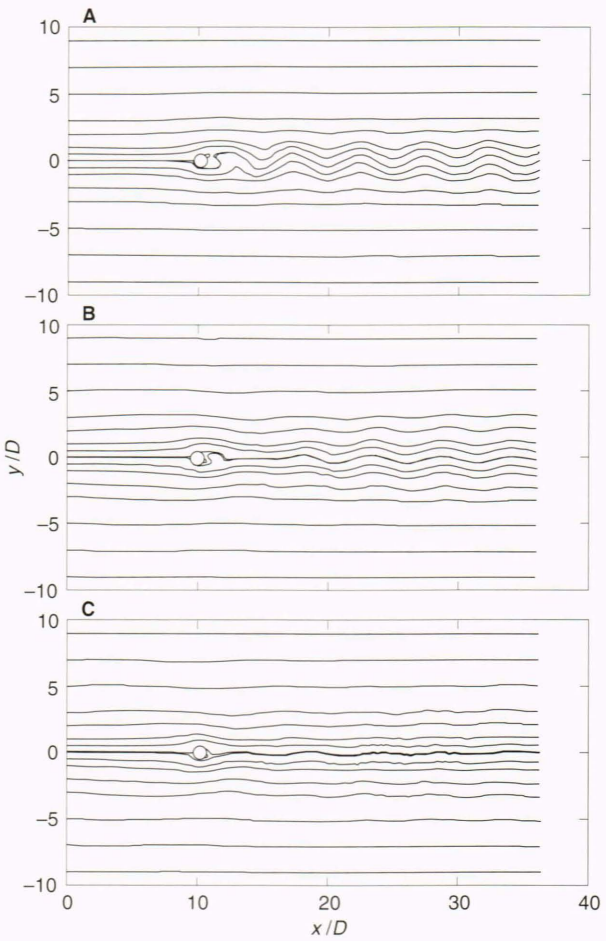

Figure 12. The flow over a moving cylinder at a Reynolds number of 100 and various Froud numbers (*Fr*). **A**. $Fr = \infty$. **B**. $Fr = 1.15$. **C**. $Fr = 0.77$. D is the diameter of the cylinder.

REFERENCES

[1] Peyret, R., and Taylor, T. D., *Computational Methods for Fluid Flow*, Springer-Verlag, Berlin (1983).

[2] Canuto, C., Hussaini, M. Y., Quarteroni, A., and Zang, T. A., *Spectral Methods in Fluid Dynamics*, Springer-Verlag, Berlin (1987).

[3] Chorin, A. J., "Numerical Solution of the Navier–Stokes Equations," *Math. Comp.* **22**, 745–762 (1968).

[4] Ku, H.-C., Rosenberg, A. P., and Taylor, T. D., "High-Order Time Integration Scheme and Preconditioned Residual Method for Solution of Incompressible Flow in Complex Geometries by the Pseudospectral Element Method," in *Proc. Twelfth Conf. on Numerical Methods in Fluid Dynamics*, Oxford, pp. 223–227 (1990).

[5] Hestenes, M. R., and Stiefel, E., "Methods of Conjugate Gradients for Solving Linear Systems," *J. Res. Natl. Bur. Stand.* **49**, 409–436 (1952).

[6] Wong, Y. S., Zang, T. A., and Hussaini, M. Y., "Preconditioned Conjugate Residual Methods for the Solution of Spectral Methods," *Comput. Fluids* **14**, 85–95 (1986).

[7] Ku, H.-C., Hirsh, R. S., and Taylor, T. D., "Simulation of Viscous Fingering by the Pseudospectral Matrix Element Method," in *Proc. Tenth Reservoir Simulation*, Houston, pp. 481–492 (1989).

[8] Ku, H.-C., Hirsh, R. S., Taylor, T. D., and Rosenberg, A. P., "A Pseudospectral Matrix Element Method for Solution of Three-Dimensional Incompressible Flows and Its Parallel Implementation," *J. Comput. Phys.* **83**, 260–291 (1989).

[9] Fox, D. G., and Orszag, S. A., "Pseudospectral Approximation to Two-Dimensional Turbulence," *J. Comput. Phys.* **11**, 612–619 (1973).

[10] Gordon, W. J., and Hall, C. A., "Transfinite Element Methods: Blending Function Interpolation over Arbitrary Curved Element Domains," *Numer. Math.* **21**, 109–129 (1973).

[11] Gordon, W. J., *Approximations with Special Emphasis on Spline Functions*, Schoenberg, I. J. (ed.), Academic Press, New York (1969).

[12] Giddens, D. P., Zarins, C. K., Glagov, S., Bharadvaj, B. K., and Ku, D. N., "Flow and Atherogenesis in the Human Carotid Bifurcation," in *Proc. Fluid Dynamics as a Localizing Factor for Atherosclerosis*, Schettler, G., et al. (eds.), Springer-Verlag, Berlin (1983).

[13] Wu, J., "Mixed Region Collapse with Internal Wave Generation in a Density-Stratified Medium," *J. Fluid Mech.* **35**, 531–544 (1969).

ACKNOWLEDGMENT: This work was partially supported by the Office of Naval Research under contract number N00039-89-C-001.

THE AUTHORS

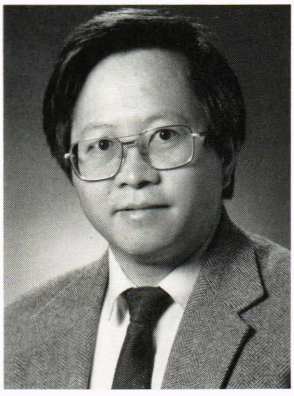

HWAR-CHING KU received a B.S. degree in chemical engineering from Tsing Hua University in 1976, an M.S. degree in chemical engineering from Taiwan University in 1980, and a Ph.D. degree in chemical engineering from the Illinois Institute of Technology in 1984. He came to APL in 1985 as a research associate in the Computational Physics Group of the Research Center, and was promoted to the Senior Staff in 1987. His current research interests include numerical methods for computational fluid dynamics studies of stratified flow around moving objects. Dr. Ku is a referee for three major journals.

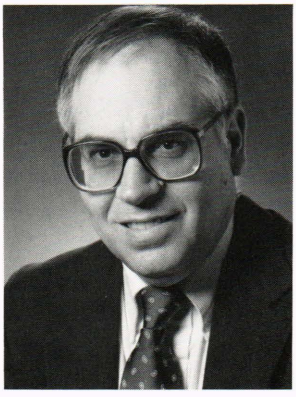

ALLAN P. ROSENBERG is a physicist in the Low Frequency Active Acoustics Group of APL's Submarine Technology Department. He received a B.S. degree from MIT in 1963 and a Ph.D. from Duke University in 1970, both in physics. He has been at APL since 1980, first as a subcontractor and more recently as a staff member. Most of his work at APL has been in the area of scientific programming.